RSC Advances

PAPER

View Article Online
View Journal | View Issue

Cite this: *RSC Adv.*, 2025, **15**, 31548

Novel guanidine derivatives as mechanistic scaffolds for anticancer agents: synthesis, characterization, DNA-binding, and computational studies

Hina Zaman,[a] Aamer Saeed, *[a] Uzma Azam, [a] Ghulam Shabir,[a] Madiha Irfan,[b] Basant Farag [c] and Hesham R. El-Seedi[d]

Cancer continues to be a major global health challenge, necessitating the ongoing development of novel small-molecule therapeutics that can selectively target DNA and disrupt cancer cell proliferation. In this study we report the synthesis and characterization of novel guanidine derivatives (**7a–j**). Their DNA-binding potential was assessed through electronic absorption spectroscopy, revealing characteristic hypochromic shifts indicative of minor groove-binding interactions with salmon sperm DNA (SS-DNA). Among the series, 4-Me, 4-Br-substituted compound (**7i**) exhibited the highest binding constant (K_b = 3.49 × 10^5 ± 0.04 M^{-1} at 298 K), comparable to that of the reference groove binder, cabozantinib (K_b = 5.79 × 10^5 M^{-1}). The negative Gibbs free energy change (ΔG = −31.61 kJ mol^{-1}) confirmed the spontaneity and thermodynamic stability of the binding interaction. Molecular docking studies further supported these experimental findings, with compound (**7i**) displaying a favorable docking score of −8.9 kcal mol^{-1} and forming hydrogen bonding and hydrophobic interactions within the DNA minor groove. Additionally, DFT calculations and ADMET predictions provided insights into the electronic features and pharmacokinetic attributes of novel guanidine derivatives (**7a–j**), establishing DNA binding as a mechanistic foundation and reinforcing their rationale for future evaluation in anticancer drug discovery.

Received 3rd August 2025
Accepted 24th August 2025

DOI: 10.1039/d5ra05647k

rsc.li/rsc-advances

1. Introduction

Cancer is a multifaceted disease marked by abnormal and uncontrolled proliferation of cells, often resulting from genetic mutations that disrupt normal cellular function.[1] Being a major cause of mortality worldwide, it continues to pose a significant challenge to global health, prompting ongoing efforts to discover more effective therapeutic strategies.[2] Among the various molecular targets explored in anticancer research, DNA has emerged as a critical focus due to its central role in regulating cell growth, division, and survival.[3]

Small molecules which exhibit DNA-binding properties have gained substantial attention for their ability to interfere with essential biological processes such as replication, transcription, and gene expression.[4] These interactions typically mediated through intercalation, groove binding or electrostatic forces can induce cytotoxic effects in cancer cells, making DNA a valuable target in chemotherapy.[5] The development of such agents holds great promise for expanding the arsenal of anticancer therapies.

Guanidines are nitrogen-rich small organic molecules that have attracted considerable attention due to their broad spectrum of biological activities.[6,7] Their significance in drug design stems from their capacity to engage in non-covalent interactions with various molecular targets, particularly through hydrogen bonding, charge pairing, and cation–π interactions with anionic groups such as carboxylates, phosphates, and sulfides.[8] These interaction patterns play a pivotal role in molecular recognition and support the pharmacological adaptability of guanidine-based compounds. A noteworthy advantage of the guanidine moiety is its amphoteric character, allowing it to function as both a Brønsted base and a mild acid.[9] Guanidine-containing drugs have demonstrated therapeutic potential across diverse areas, including antibacterial, antifungal, antiprotozoal, antiviral and anticancer applications (Fig. 1).

Although DNA remains one of the primary targets of guanidine-based agents, their cytotoxic mechanisms extend beyond DNA interaction.[10,11] These include disruption of

[a]*Department of Chemistry, Quaid-I-Azam University, Islamabad, 45320, Pakistan. E-mail: asaeed@qau.edu.pk; Fax: +92-51-9064-2241; Tel: +92-51-9064-2128*

[b]*Institute of Chemistry, Khawaja Fareed University of Engineering and Information Technology, Rahim Yar Khan, 64200, Pakistan*

[c]*Department of Chemistry, Faculty of Science, Zagazig University, Zagazig 44519, Egypt*

[d]*Department of Chemistry, Faculty of Science, Islamic University of Madinah, Madinah, 42351, Saudi Arabia*

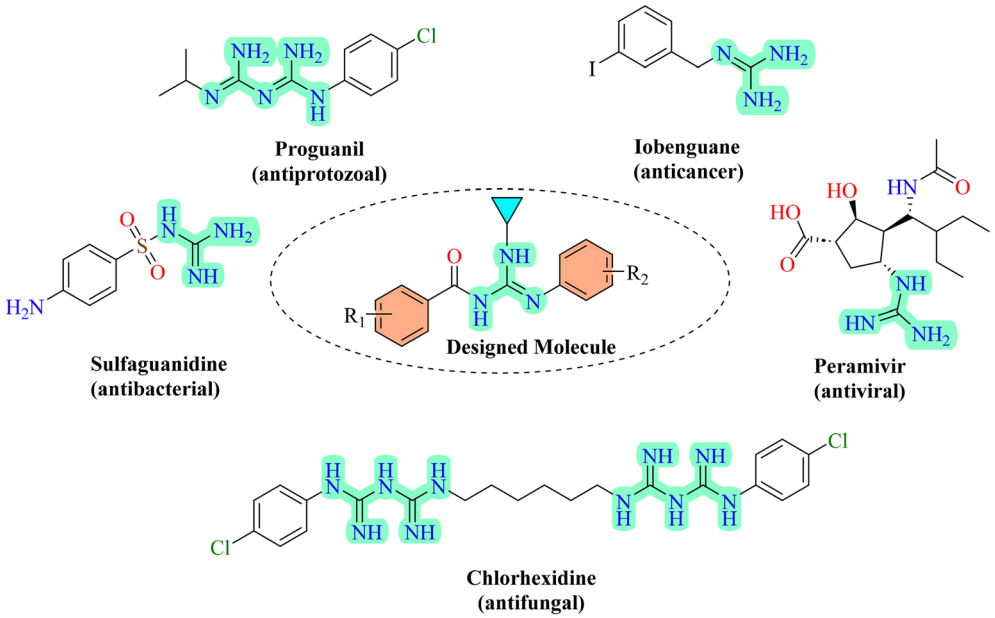

Fig. 1 Some selected guanidine incorporating drugs and designed molecule.

bacterial membranes, induction of reactive oxygen species (ROS), mitochondrial-mediated apoptosis, and inhibition of proteins.[12] The guanidine group is therefore considered a privileged scaffold in anticancer drug development. Its ability to interact with phosphate residues within the minor groove of DNA helix enhances its potential as a DNA-binding pharmacophore.[13,14]

In response to the pressing need for effective anticancer therapies and the recognized biological versatility of guanidines, we designed and synthesized a series of novel cyclopropyl-linked guanidine derivatives (**7a–j**) as part of our ongoing research.[15–17] To the best of our knowledge, the synthesis of cyclopropyl-linked guanidines has not been previously reported, making this scaffold itself a novel contribution in guanidine-based drug discovery. The cyclopropyl ring is a conformationally constrained and lipophilic bioisostere, frequently employed in drug design to enhance metabolic stability, restrict conformational flexibility, and modulate molecular recognition at biological targets.[18] Its incorporation into guanidine scaffolds offers a distinct steric and electronic environment that has not been rigorously explored in DNA binding studies. Although guanidines have been widely studied for biological activity, systematic studies on cyclopropyl-appended guanidines, particularly their DNA-binding potential and structure–activity relationships, are scarce. To address this gap, the present work combines novel synthetic development with experimental DNA-binding studies and computational analyses to provide an integrated evaluation of their pharmacological relevance. Specifically, we investigated their binding constants (K_b), thermodynamic stability (ΔG), and spectroscopic behaviour, while correlating these results with DFT-derived electronic descriptors, molecular docking simulations, and ADMET predictions. This dual approach not only clarifies how substituent and electronic features influence DNA-binding efficiency but also positions cyclopropyl-linked guanidines as a previously unexplored and promising class of DNA-targeted anticancer agents.

2. Results and discussion

2.1. Chemistry

The novel guanidine derivatives (**7a–j**) were synthesized following the previously reported method with slight modifications, as outlined in Scheme 1. Initially, the corresponding thiourea intermediates[19] (**5a–d**) were subjected to a desulfurization reaction by treating them with mercuric chloride in the presence of triethylamine as a base. This reaction facilitates the removal of the sulfur atom from the thiourea moiety. Subsequently, various substituted anilines (**6a–f**) were introduced into the reaction mixture, leading to nucleophilic substitution at the electrophilic intermediate generated *in situ*. The reaction proceeded smoothly under mild conditions to afford the targeted guanidine derivatives (**7a–j**) in excellent yields.

The structural characterization for synthesized compounds (**7a–j**) was carried out through different spectroscopic techniques *i.e.* FTIR and NMR. The spectral data of a representative derivative, (**7a**), are discussed below:

The FTIR spectrum of the compound (**7a**) displayed characteristic N–H stretching bands at 3346 and 3214 cm^{-1}. A band at 3088 cm^{-1} was indicative of sp^2 C–H stretching, whereas the absorption at 3010 cm^{-1} corresponded to sp^3 C–H vibrations. Similarly, a strong band at 1678 cm^{-1} confirmed the presence of an amide carbonyl group, and the peak at 1643 cm^{-1} was attributed to C=N stretching. The C=C stretching vibrations appeared at 1544 cm^{-1}, and a band at 1341 cm^{-1} was associated with C–N stretching.

In ^1H NMR spectrum, the amide proton appeared as a broad singlet at 10.82 ppm, indicative of the deshielding effect caused

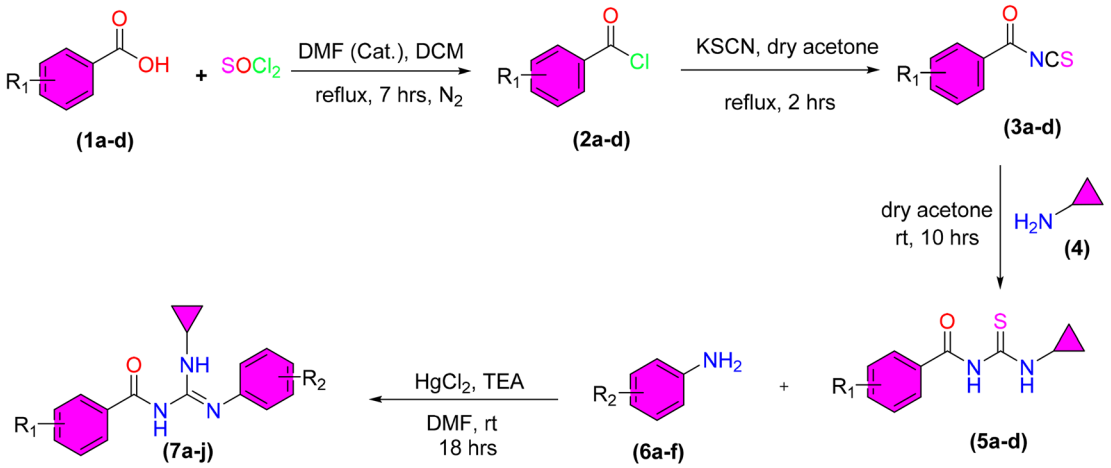

7a; R_1 = H, R_2 = 4-Cl **7b**; R_1 = H, R_2 = 4-Br **7c**; R_1 = H, R_2 = 4-CH_3
7d; R_1 = H, R_2 4-OCH_3 **7e**; R_1 = H, R_2 = 3,4,5-triCH_3 **7f**; R_1 = H, R_2 = 3-NO_2
7g; R_1 = 4-OCH_3, R_2 = 4-Cl **7h**; R_1 = 4-CH_3, R_2 = 4-Cl **7i**; R_1 = 4-CH_3, R_2 = 4-Br
7j; R_1 = 3,4-diOCH_3, R_2 = 4-Cl

Scheme 1 Synthetic trail of novel guanidine derivatives (**7a–j**).

by the adjacent carbonyl group. The broadness of the signal suggested the possibility of hydrogen bonding or exchange with the solvent or other protons. Similarly, the N–H proton attached to the cyclopropyl ring also appeared as a broad singlet, but at a slightly lower chemical shift of 8.40 ppm. The methine proton of the cyclopropyl was observed as a multiplet in the range of 2.92–2.83 ppm. The remaining four protons appeared as two distinct multiplets between 0.98 and 0.81 ppm. Additionally, all protons of the phenyl rings were observed in the range of 8.15–7.36 ppm. The ^{13}C NMR spectrum further supported the structure, showing the most deshielded signal at 176.7 ppm for the amide carbonyl carbon, and a characteristic signal at 160.0 ppm for the imine carbon. The cyclopropyl ring carbons appeared at 22.2 and 7.2 ppm, while aromatic carbons were recorded within the range of 138.9–125.4 ppm. All these spectral details confirmed the successful synthesis of the desired guanidine derivative.

2.2. DNA binding studies

Numerous anticancer drugs target DNA as their primary pharmacological site. Compounds that interact with genomic DNA have demonstrated notable therapeutic success.[20] Therefore, assessing the interaction between newly synthesized compounds (**7a–j**) and DNA is crucial for elucidating their mechanism of action and anticancer potential. The interaction of guanidine derivatives with salmon sperm DNA (SS-DNA) was evaluated using UV-Visible spectroscopy. Absorption spectra for each compound (50 μM) were recorded in the absence and then increasing the concentrations of SS-DNA, (5–40 μM) (Fig. S31). Prior to measurements, the compound–DNA mixtures were incubated at room temperature for thirty to forty minutes to allow for interaction. All parameters of DNA-binding are illustrated in Table 1. The synthesized compounds (**7a–j**) displayed characteristic absorption bands in the range of 236–283 nm, corresponding to π–π* transitions. Upon the incremental addition of SS-DNA, hypochromism with minimal or absence of significant shifts in λ_{max} was observed in the UV-Vis spectra of all compounds, implying effective binding to DNA. The absence of significant shifts in λ_{max} (<10 nm), and the observed hypochromic effect suggest a groove binding mode, characterized by electronic overlap between the chromophores of the compounds and DNA base pairs within the minor groove.

To quantify the binding interaction, the intrinsic binding constant (K_b) was determined using the Benesi–Hildebrand method and Gibbs free energy (ΔG) was calculated. The K_b values ranged from 10^4 to 10^5 M^{-1}, consistent with minor groove binder, cabozantinib (10^5 M^{-1}).[21] The order of DNA-binding affinity, based on K_b values, was: **7i** > **7e** > **7a** > **7f** > **7g** > **7c** > **7j** > **7h** > **7d** > **7b**. These results support a minor groove-binding mode rather than intercalation in accordance with previously reported guanidine-based molecules.[22] Among these, compound (**7i**) (R_1 = 4-Me, R_2 = 4-Br) exhibited the highest K_b ($3.49 \times 10^5 \pm 0.04$ M^{-1}) which is comparable to the reference drug cabozantinib and the most negative ΔG value (-31.61 kJ mol^{-1}), reflecting a strong and spontaneous binding affinity. This enhanced interaction is likely due to the synergistic electronic and hydrophobic effects of the methyl and bromo substituents. Compound (**7e**), with 3,4,5-trimethylphenyl ring, also showed strong binding ($K_b = 9.68 \times 10^4 \pm 0.08$ M^{-1}, $\Delta G = -28.43$ kJ mol^{-1}), suggesting that electron-donating methyl groups enhance DNA interaction through hydrophobic and van der Waals forces (Fig. 2). Moderate to high DNA-binding affinities were observed for halogen- and nitro-

Table 1 Comparative DNA binding affinities and thermodynamic data of guanidine derivatives (**7a–j**)

Compd	R_1, R_2	λ_{max} (nm)	$\Delta\lambda$ (nm)	K_b (M^{-1})	ΔG (kJ mol^{-1})
7a	H, 4-Cl	274	2	$7.84 \times 10^4 \pm 0.16$	−27.91
7b	H, 4-Br	236	—	$1.33 \times 10^4 \pm 0.03$	−23.52
7c	H, 4-Me	272	2	$5.21 \times 10^4 \pm 0.12$	−26.90
7d	H, 4-OMe	271	3	$2.37 \times 10^4 \pm 0.23$	−24.95
7e	H, 3,4,5-triMe	270	2	$9.68 \times 10^4 \pm 0.08$	−28.43
7f	H, 3-NO_2	261	—	$7.07 \times 10^4 \pm 0.10$	−27.65
7g	4-OMe, 4-Cl	274	—	$5.74 \times 10^4 \pm 0.05$	−27.14
7h	4-Me, 4-Cl	283	7	$2.90 \times 10^4 \pm 0.13$	−25.45
7i	4-Me, 4-Br	259	—	$3.49 \times 10^5 \pm 0.04$	−31.61
7j	3,4-diOMe, 4-Cl	274	3	$4.30 \times 10^4 \pm 0.14$	−26.42
Cabozantinib	—	—	—	5.79×10^5	−32.87

substituted derivatives such as (**7a**), (**7f**), and (**7g**), with K_b values between 5.74×10^4 and 7.84×10^4 M^{-1} and corresponding negative ΔG values, signifying spontaneous binding. These interactions may be stabilized through hydrogen bonding and electrostatic forces. In contrast, compound (**7b**) (4-Br) showed the lowest K_b ($1.33 \times 10^4 \pm 0.03$ M^{-1}) and the least negative ΔG (−23.52 kJ mol^{-1}), implying a weaker interaction. This may result from steric hindrance or suboptimal orientation for groove binding.

To better contextualize the DNA-binding properties of (**7i**), we compared its binding constant and docking score with several clinically or experimentally relevant DNA-binding agents (Table 2). Metformin, a widely used biguanide antidiabetic drug, binds DNA with moderate affinity ($K_b \approx 8.3 \times 10^4$ M^{-1}) but shows no direct anticancer activity. Amiloride, an FDA-approved diuretic drug, exhibits very weak binding ($K_b \approx 10^2$ M^{-1}) and only limited indirect anticancer effects.[23] In contrast, netropsin, a well-established DNA minor-groove binder, displays strong affinity ($K_b \approx 10^4$ to 10^5 M^{-1}) and docking scores in the range of −8 to −9 kcal mol^{-1}, with reported antimicrobial and experimental anticancer activity.[24] Against this benchmark set, (**7i**) exhibits a competitive binding profile, underscoring the novelty of our scaffold within guanidine-derived chemotypes and its potential as a DNA-interactive therapeutic lead.

Overall, the DNA-binding data confirm that the electronic nature and position of the substituents significantly influence the interaction strength of guanidine derivatives with DNA. The spontaneous nature of all interactions (as shown by negative ΔG values) supports the potential of these compounds as DNA-targeting anticancer agents.

2.3. Density functional theory (DFT) analyses

DFT offers crucial information on the electronic structure, stability, and reactivity of compounds, which is fundamental for understanding their interactions with different biological targets.[25] In this study, DFT calculations were performed for

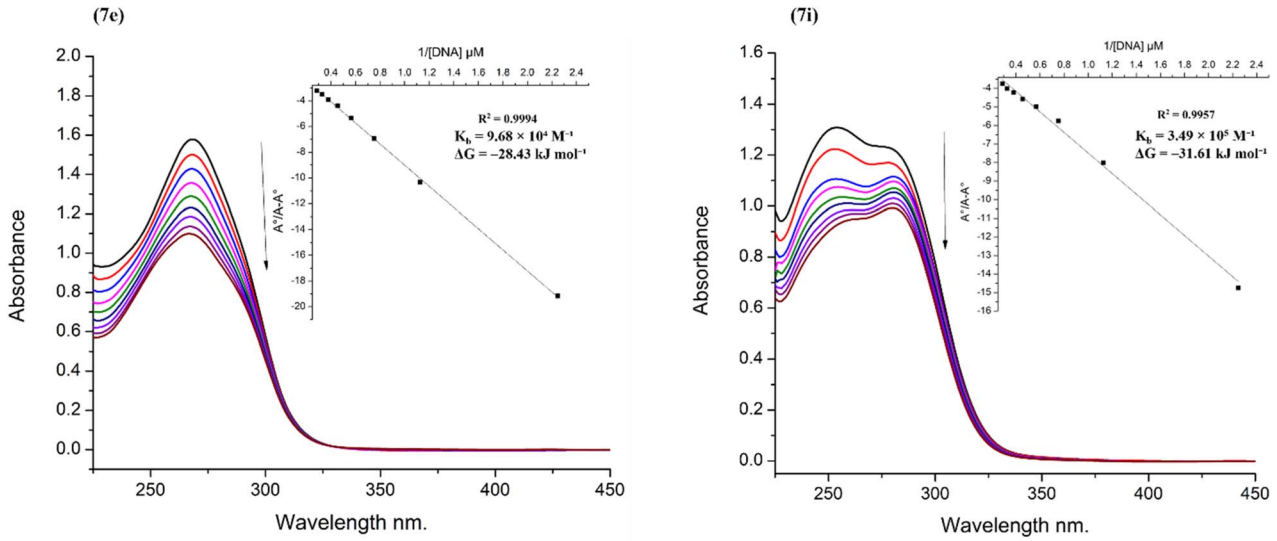

Fig. 2 UV-Vis absorption spectra of the most active compounds (**7e**) ($R^2 = 0.9994$) and (**7i**) ($R^2 = 0.9957$) (50 µM) in the absence and in the presence of SS-DNA (5–40 µM); (inset) plot of $A_o/A - A_o$ *versus* 1/[DNA] µM. The decrease in the absorption of compounds with increasing concentrations of SS-DNA in the absorption spectra at pH 7.0 and temperature 298 K indicate the hypochromic effect.

Table 2 Comparative DNA-binding parameters of compound (**7i**) and reference agents

Molecule	Reported biological role	K_b (M^{-1})	Docking score (kcal mol^{-1})
7i (this work)	—	$\sim 1.2 \times 10^5$	−7.6
Metformin	Antidiabetic	8.3×10^4	−5.2
Amiloride	Diuretic, Na^+ channel blocker	$\sim 10^2$	−4.8
Netropsin	Antimicrobial and anticancer	10^4 to 10^5	−8.2 to −9.0

Table 3 FMO energies and global reactivity descriptors for synthesized guanidines (**7a–j**)

Compd	R_1, R_2	E_{HOMO} (eV)	E_{LUMO} (eV)	ΔE (eV)	IP (eV)	EA (eV)	X (eV)	ω (eV)	η (eV)	S (eV^{-1})
7a	H, 4-Cl	−5.5	−1.51	3.99	5.5	1.51	3.50	3.07	1.99	0.50
7b	H, 4-Br	−5.52	−1.39	4.12	5.52	1.39	3.46	2.90	2.06	0.48
7c	H, 4-Me	−5.34	−1.27	4.07	5.34	1.27	3.30	2.68	2.03	0.49
7d	H, 4-OMe	−5.38	−1.32	4.06	5.38	1.32	3.35	2.77	2.03	0.49
7e	H, 3,4,5-triMe	−5.11	−1.24	3.87	5.11	1.24	3.17	2.60	1.93	0.51
7f	H, 3-NO_2	−5.89	−2.42	3.47	5.89	2.42	4.15	4.97	1.73	0.57
7g	4-OMe, 4-Cl	−5.52	−1.19	4.33	5.52	1.19	3.35	2.60	2.16	0.46
7h	4-Me, 4-Cl	−5.52	−1.37	4.14	5.52	1.37	3.44	2.86	2.07	0.48
7i	4-Me, 4-Br	−4.98	−1.26	3.71	4.98	1.26	3.12	2.63	1.85	0.53
7j	3,4-diOMe, 4-Cl	−5.57	−1.35	4.21	5.57	1.35	3.46	2.85	2.10	0.47

guanidine based compounds (**7a–j**) and the global reactivity parameters are presented in Table 3. Frontier molecular orbital (FMO) analysis is a widely recognized quantum chemical method employed to explore the electronic attributes of organic molecules. According to FMO theory, the highest occupied molecular orbital (HOMO) and the lowest unoccupied molecular orbital (LUMO) play a crucial role in determining a compound's chemical behavior, including its reactivity and stability. The FMO distribution patterns of the most active compounds in the series (**7e** and **7i**) are illustrated in Fig. 3, highlighting the key regions likely involved in effective biological interactions.

A higher E_{HOMO} value reflects strong electron donating capacity and is directly associated with a lower ionization potential (IP). Among the examined compounds, (**7d**) exhibited the highest E_{HOMO} (−4.9 eV) and the lowest IP (4.9 eV), indicating its strong electron-donating nature. In contrast, a lower E_{LUMO} value is linked to greater electron affinity (EA). Notably, compound (**7f**) displayed the highest EA (2.42 eV) and the lowest E_{LUMO} (−2.42 eV), highlighting its strong tendency to accept electrons.

The energy gap between HOMO–LUMO (ΔE) is a critical parameter that affects both the chemical reactivity and stability of molecules. A smaller ΔE indicates higher reactivity and

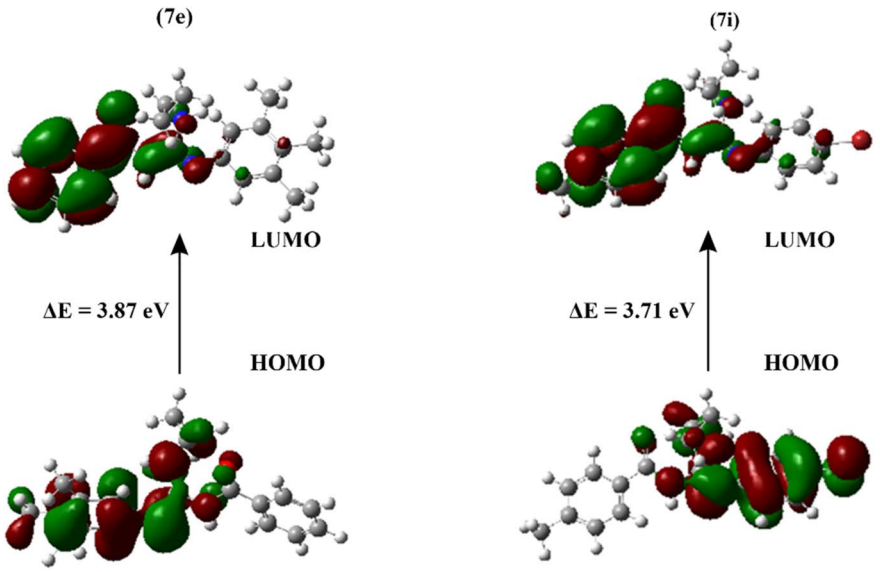

Fig. 3 FMO's of the most active guanidine derivatives (**7e** and **7i**).

a greater potential for interactions with biological targets. Among the synthesized derivatives, (**7f**), (**7i**), and (**7e**), displayed the lowest energy gaps (3.47, 3.71, and 3.87 eV, respectively). In contrast, compound (**7g**) showed the highest energy gap of 4.33 eV, reflecting greater stability and reduced reactivity.

The synthesized derivatives (**7a–j**) displayed moderate electronegativity (X) values ranging from 3.12 to 4.15 eV, reflecting a balanced ability to accept electrons and a potential affinity for DNA binding.

The electrophilicity index (ω), a key indicator of a molecule's reactivity toward electron-rich sites in biological targets, was highest for compounds (**7a**) (3.07 eV), (**7b**) (2.90 eV), and (**7f**) (4.97 eV). These elevated values suggest a strong electron-accepting capacity, implying higher reactivity and lower inherent stability for these molecules.

The chemical hardness (η) analysis showed that compound (**7g**) possessed the highest hardness value (2.16 eV), suggesting strong resistance to charge transfer and low chemical reactivity. While the chemical softness (S), the reciprocal of hardness, was greatest for compound (**7f**) (0.77 eV^{-1}), indicating its higher reactivity and greater susceptibility to electronic interactions. Moreover, Molecular Electrostatic Potential map (MEP) provided valuable information on the electron distribution within the compounds, showcasing electron-rich (red) and electron-deficient (blue) regions that are likely to participate in nucleophilic and electrophilic interactions with biological targets. The MEP map of one of the most active compounds (**7i**), depicted in Fig. 4, clearly illustrates these reactive regions involved in binding interactions. Collectively, these findings support the potential of these compounds to interact effectively with DNA and serve as promising anticancer agents.

2.4. Quantitative correlation analysis of DFT descriptors

To strengthen the qualitative frontier orbital analysis, quantitative correlations were established between the electronic descriptors (E_{HOMO}, E_{LUMO}, ΔE) and the experimental binding constants (K_b) and docking scores (Fig. 5a–e). Regression analysis revealed that ΔE exhibited a moderate negative correlation with $\log_{10}(K_b)$ ($r = -0.54$; Fig. 5a), reflecting that a smaller orbital gap enhances reactivity and promotes stronger DNA binding. E_{HOMO} correlated moderately and positively with $\log_{10}(K_b)$ ($r = +0.51$; Fig. 5b), consistent with enhanced donor capability supporting groove interactions, whereas E_{LUMO} alone showed negligible correlation ($r \approx -0.02$; Fig. 5c).

Docking scores showed a moderate negative correlation with $\log_{10}(K_b)$ ($r = -0.50$; Fig. 5d), indicating that stronger DNA binders also tend to display more favorable docking energies. Importantly, ΔE exhibited a stronger positive correlation with docking scores ($r = +0.65$; Fig. 5e), reinforcing that electronic reactivity descriptors are mechanistically linked with molecular recognition trends observed in docking.

The Pearson correlation matrix (Fig. 5f) statistically summarizes these relationships, confirming that ΔE and E_{HOMO} are the strongest electronic predictors of DNA binding affinity in this series, while E_{LUMO} is non-informative. Moreover, ΔG correlated moderately with both ΔE ($r \approx -0.49$) and docking scores ($r \approx -0.52$), suggesting that thermodynamic stability is also partially governed by electronic descriptors. Collectively, these statistical analyses provide a quantitative framework to support the SAR trends observed experimentally, thereby addressing the limitations of purely qualitative DFT interpretation.

2.5. Molecular docking

In the development of anticancer agents, the ability of a compound to bind DNA is a critical factor, as such interactions enable the identification of specific DNA regions targeted through non-covalent mechanisms.[21] Molecular docking serves as a powerful computational tool, especially when integrated with experimental data, to predict binding affinity and interaction patterns of potential drug candidates.[26] In this study, AutoDock Vina was utilized to evaluate the binding modes and

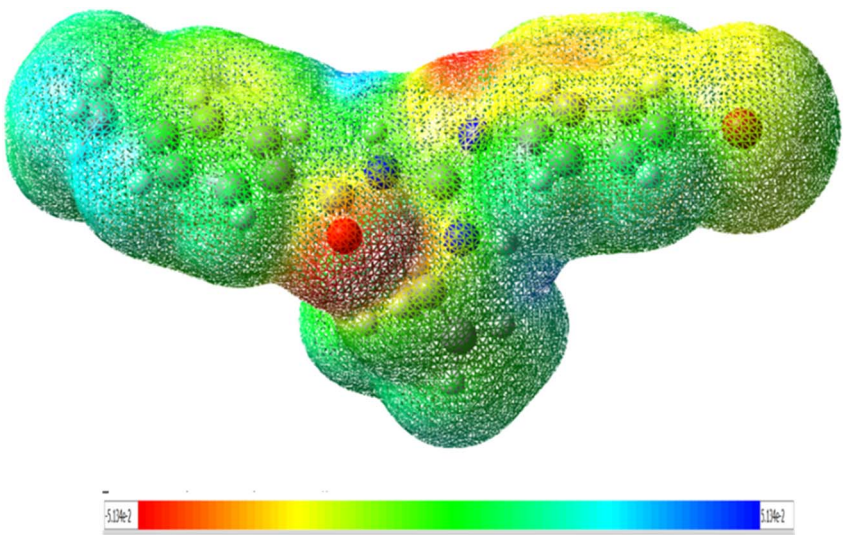

Fig. 4 MEP map of guanidine derivative (**7i**).

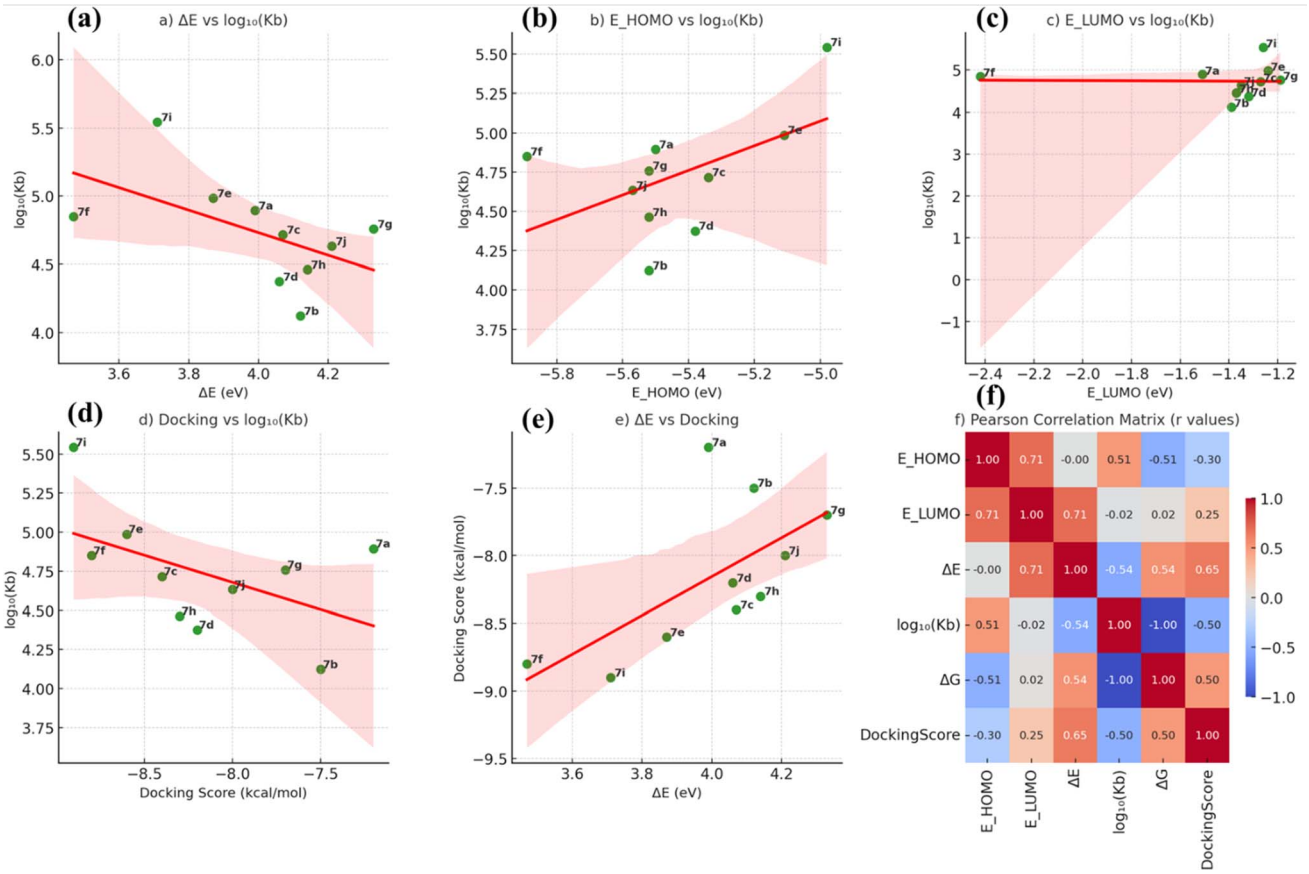

Fig. 5 Multi-panel analysis of electronic descriptors and DNA binding/docking parameters. Panels (a–e) illustrate regression plots correlating ΔE, E_{HOMO}, E_{LUMO}, and docking score with $\log_{10}(K_b)$, as well as ΔE with docking score. Panel (f) provides a Pearson correlation matrix summarizing interrelationships among all descriptors and binding data.

affinities of the synthesized guanidines (**7a–j**) toward double-stranded DNA (PDB ID: 3EY0), sequence: 5′-(ATATATATAT)-3′. The docking results summarized in Table 4, revealed that all compounds interacted effectively with the DNA duplex, exhibiting binding energies between −7.2 and −8.9 kcal mol^{-1}, implying their potential for stable DNA binding. Docking simulations of compounds (**7a–j**) demonstrated their preferential binding within the minor groove of the DNA helix, as illustrated in Fig. 6. Among all synthesized guanidine derivatives, (**7i**) bearing 4-methyl and 4-bromo substituents demonstrated the strongest binding energy (−8.9 kcal mol^{-1}), suggesting a highly stable interaction within the DNA minor groove. This was closely followed by compound (**7f**) (3-nitro) with −8.8 kcal mol^{-1} and (**7e**) (3,4,5-trimethyl) with −8.6 kcal mol^{-1}, revealing that both electron-donating and electron-withdrawing groups can enhance DNA binding when positioned appropriately. Most compounds formed conventional hydrogen bonds with adenine (DA-A, DA-B) and thymine (DT-A, DT-B) residues. The hydrogen bond distances generally fell within the optimal range of 2.1–2.7 Å, indicating stable binding. Compound (**7e**), for instance, formed strong conventional hydrogen bonds with DA-A:7 and DA-B:5 at 2.73 and 2.66 Å, respectively. Similarly, (**7c**) (R_1 = H, R_2 = 4-Me) demonstrated a binding energy of −8.4 kcal mol^{-1} and formed multiple H-bonding interactions with DA-B:7 and DA-A:7.

In addition to hydrogen bonding, many compounds exhibited carbon hydrogen bonds and hydrophobic interactions such as π–anion, π–alkyl, and π–sigma contacts. These non-covalent interactions further stabilized the compound–DNA complexes. The compound (**7h**) (4-Me, 4-Cl) exhibited a significant binding energy of −8.3 kcal mol^{-1} and engaged in multiple non-covalent interactions including hydrogen bonding with DA-A:7, carbon hydrogen bonding, π–anion interaction with DT-B:6, and π–alkyl interactions with DA-A:7 and DA-B:5, respectively. Likewise, (**7d**) (H, 4-OMe) displayed similar interactions, reinforcing its relatively strong binding energy of −8.2 kcal mol^{-1}. The presence of halogen atoms appears to contribute positively to π-related interactions. For example, compound (**7b**) (R_1 = H, R_2 = 4-Br) formed π–alkyl interactions in addition to conventional and carbon hydrogen bonding, resulting in a moderate binding energy of −7.5 kcal mol^{-1}. In comparison, (**7a**) (H, 4-Cl) showed the weakest binding (−7.2 kcal mol^{-1}), forming fewer interactions and lacking significant hydrophobic contacts. Compound (**7f**), bearing a nitro group, showed one of the highest binding affinities. It formed a conventional hydrogen bond with DA-A:5 and engaged in additional carbon hydrogen and π–sigma interactions with DT-B:8 and DA-A:7, respectively, which may be

Table 4 Docking results of synthesized guanidines (7a–j)

Compd	R_1, R_2	Binding energy	Distance	Interacting residue	Type of interactions
7a	H, 4-Cl	−7.2	2.25, 2.36	DA-B:7, DT-B:8	Conv. H-bond
			3.55	DT-B:8	Carbon hydrogen bond
7b	H, 4-Br	−7.5	2.11	DA-A:7	Conv. H-bond
			3.08	DA-A:7	Carbon hydrogen bond
			5.49, 5.27, 5.17	DA-B:5, DA-A:7, DA-A:7	π–alkyl
7c	H, 4-Me	−8.4	2.71, 2.52	DA-B:7, DA-A:7	Conv. H-bond
				DT-B:6	Carbon hydrogen bond
7d	H, 4-OMe	−8.2	3.51	DT-A:8	Carbon hydrogen bond
			4.39	DT-A:6	π–anion
			5.47, 5.35	DA-A:5, DA-A:7	π–alkyl
7e	H, 3,4,5-triMe	−8.6	2.73, 2.66	DA-A:7, DA-B:5	Conv. H-bond
7f	H, 3-NO_2	−8.8	2.50	DA-A:5	Conv. H-bond
			3.66	DT-B:8	Carbon hydrogen bond
			3.94	DA-A:7	π–sigma
7g	4-OMe, 4-Cl	−7.7	2.67, 2.50	DA-A:7, DA-B:5	Conv. H-bond
			3.20, 3.58, 3.55	DA-A:9, DT-B:6, DT-B:8	Carbon hydrogen bond
			4.98	DA-A:5	π–alkyl
7h	4-Me, 4-Cl	−8.3	2.12	DA-A:7	Conv. H-bond
			3.46	DA-A:7	Carbon hydrogen bond
			4.78	DT-B:6	π–anion
			5.42, 5.15	DA-B:5, DA-A:7	π–alkyl
7i	4-Me, 4-Br	−8.9	2.10	DA-A:7	Conv. H-bond
			3.43	DT-A:8	Carbon hydrogen bond
			4.80	DT-B:6	π–anion
			5.05, 5.16, 5.44	DA-A:7, DA-B:5	π–alkyl
7j	3,4-diOMe, 4-Cl	−8.0	2.13, 2.51	DA-A:7, DA-A:7	Conv. H-bond
			3.70, 3.43, 3.79	DA-A:7, DT-A:6, DT-B:6	Carbon hydrogen bond
			4.93, 4.47, 4.51, 5.21	DA-A:7, DA-B:5, DT-B:6	π–alkyl

attributed to the strong electron-withdrawing nature of the nitro group promoting polar interactions. Furthermore, (**7g**) (4-OMe, 4-Cl) also interacted *via* multiple modes, including hydrogen bonding with DA-A:7 and DA-B:5, and π–alkyl interactions, achieving a binding energy of −7.7 kcal mol^{-1}. Finally, (**7j**) (3,4-diOMe, 4-Cl) showed a binding energy of −8.0 kcal-mol^{-1} and engaged in a combination of conventional hydrogen bonding and extensive π–alkyl interactions involving DA-A:7, DA-B:5, and DT-B:6. This suggests that the di-methoxy substitution enhances van der Waals contacts and hydrophobic stabilization with the DNA grooves. Overall, these docking results correlate well with the DNA binding constants (K_b) and free energy changes (ΔG), supporting the conclusion that the synthesized guanidine derivatives effectively bind with DNA, predominantly *via* minor groove binding, involving hydrogen bonding and hydrophobic interactions. The high binding energy of (**7i**), (**7e**), and (**7f**) suggests their potential as effective DNA-targeting anticancer agents.

While SS-DNA and a canonical DNA duplex (PDB ID: 3EY0) provide useful model systems, they do not fully replicate the sequence heterogeneity and chromatin organization of human genomic DNA. Thus, the binding affinities observed for the synthesized compounds should be interpreted as indicative rather than absolute. Future studies will focus on validating these findings with human genomic DNA, complementary biophysical assays, and in chromatin contexts to better establish biological relevance.

2.6. Structure–activity relationship (SAR) analysis

A systematic SAR evaluation was carried out by correlating the electronic features (HOMO–LUMO gap, softness, electron-donating/withdrawing tendencies), steric effects, and experimental DNA-binding data (K_b, ΔG) (Fig. 7). Three major trends were observed. First, compounds with small electron-donating substituents (Me, OMe) at the *para* position generally enhanced DNA-binding affinity compared to purely bromo derivative. For example, (**7c**) (4-Me) and (**7d**) (4-OMe) displayed moderate affinities ($K_b = 5.21 \times 10^4 \pm 0.12$ and $2.37 \times 10^4 \pm 0.23$ M^{-1}), consistent with improved groove fit and stabilization through hydrophobic or weak polar contacts. Second, the synergistic effect of combining an EDG with a polarizable halogen was most evident in (**7i**) (4-Me, 4-Br), which emerged as the strongest binder in the series ($K_b = 3.49 \times 10^5 \pm 0.04$ M^{-1}; $\Delta G = -31.61$ kJ mol^{-1}). Here, the *para*-methyl group enhances hydrophobic packing and increases local electron density, while bromine contributes polarizability and favorable groove-ligand contacts. This balance of steric compatibility and electronic tuning provides an optimal fit, explaining why (**7i**) outperformed even multi-methylated analogues such as (**7e**) (3,4,5-triMe). Third, halogenation alone was insufficient: **7b** (4-Br) exhibited the weakest binding ($K_b = 1.33 \times 10^4 \pm 0.03$ M^{-1}), suggesting steric hindrance and lack of electron donation limit stabilization. Conversely, chloro substitution (**7a**, 4-Cl) gave a stronger effect ($7.84 \times 10^4 \pm 0.16$ M^{-1}), indicating that

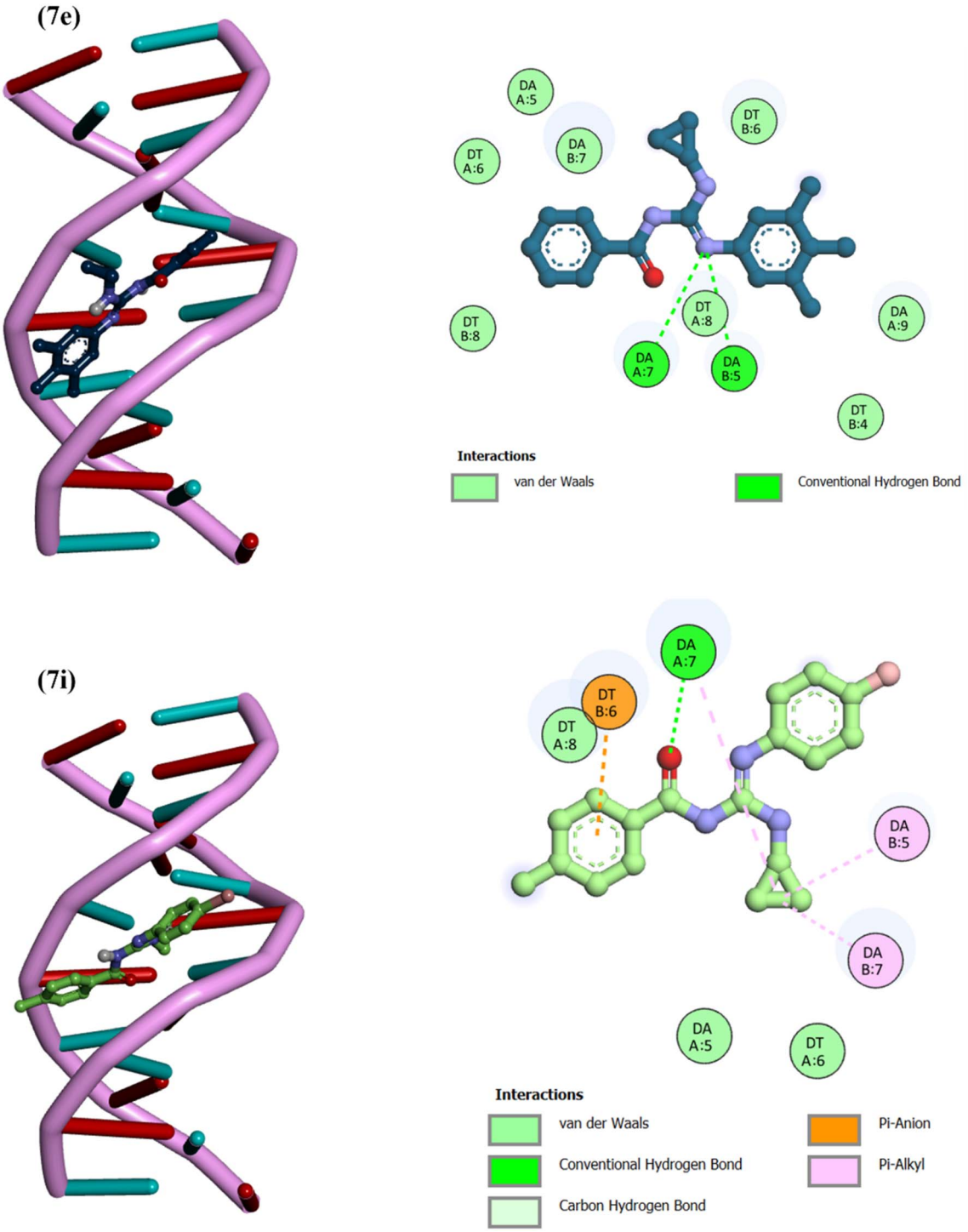

Fig. 6 3D and 2D docked pose of guanidine derivatives (**7e** and **7i**).

chlorine's smaller size and moderate polarizability favor groove accommodation.

A notable exception was observed with (**7f**) (3-NO_2), which showed a comparatively high binding constant ($K_b = 7.07 \times 10^4 \pm 0.10\ M^{-1}$), exceeding some EDG-bearing analogues. Despite being a strong electron-withdrawing group, the *meta*-NO_2 may preserve planarity and enable specific polar or electrostatic interactions within the groove. DFT data support this interpretation, as (**7f**) showed the lowest ΔE (3.47 eV) and highest S (0.77 eV^{-1}), reflecting greater electronic reactivity that could facilitate DNA interactions, even if overall stabilization is less efficient than in (**7i**).

These findings are in line with previous reports on minor groove binders, where electronic tuning through methylation

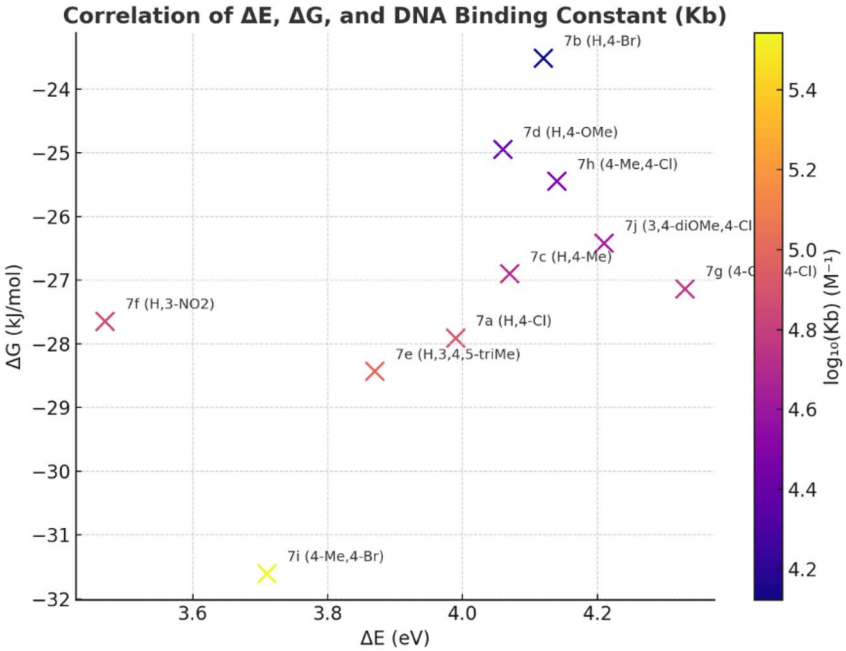

Fig. 7 Qualitative SAR visualization illustrating the influence of electronic substituents on K_b, ΔE, and ΔG in the synthesized guanidine series.

and halogenation enhances both DNA affinity and biological activity, including cytotoxic potential.[27] Notably, literature on guanidine-based minor groove binders also demonstrates that such substituent patterns not only enhance DNA binding affinity but are frequently associated with increased cytotoxic activity, attributed to improved hydrophobic contacts and stabilization of DNA–ligand complexes.[28] Taken together, our SAR analysis shows that optimal binding requires a balance of substituents: small EDGs provide enhanced groove fit, halogens contribute polarizability, and specific positioning of EWGs can occasionally create favorable polar contacts. These features explain why some synthesized guanidine derivatives achieved the strongest DNA-binding affinities in the present study.

Table 5 Pharmacokinetic parameters of synthesized guanidine derivatives (7a–j)

Compd	7a	7b	7c	7d	7e	7f	7g	7h	7i	7j
Absorption										
Caco-2 permeability	1.288	1.294	0.828	0.835	1.262	0.348	1.044	1.285	1.29	1.062
HIA	85.175	85.108	86.633	90.415	100	87.475	86.243	85.275	85.208	87.933
Distribution										
VD	1.431	1.432	1.47	0.011	0.011	1.398	1.256	1.49	1.491	1.109
BBB permeability, log BB	0.175	0.174	0.188	−0.084	0.126	0.156	0.009	0.146	0.144	0.003
CNS permeability, log PS	−1.85	−1.827	−1.89	−3.277	−2.042	−2.173	−3.299	−1.779	−1.757	−2.226
Metabolism										
CYP1A2	—	—	—	—	—	—	—	—	—	Inhibitor
CYP2C19	—	—	—	—	—	Inhibitor	Inhibitor	—	—	Inhibitor
CYP2C9	—	—	—	—	—	—	—	—	—	—
CYP2D6	—	—	—	—	—	—	—	Inhibitor	Inhibitor	Inhibitor
CYP3A4	Substrate	Substrate	Substrate	—	—	Substrate/inhibitor	Substrate	Substrate	Substrate	—
Excretion										
CL_{plasma}	−0.43	0.809	0.841	0.86	−0.57	0.539	0.85	0.831	0.811	0.853
Toxicity										
Herg blockers	No	No	No	No	No	No	No	No	No	No
AMES toxicity	No	No	Yes	No	No	Yes	No	Yes	No	No
Skin sensitization	No	No	No	No	No	No	No	No	No	No
Human hepatotoxicity	No	No	No	No	No	No	Yes	No	No	No

2.7. ADMET profiling

ADMET profiling was carried out using online web tools, pkCSM and ADMETlab 3.0, to assess the pharmacokinetic behavior of the synthesized guanidine derivatives (**7a–j**). The results presented in Table 5, highlight drug-likeness and pharmacokinetic attributes, supporting their potential as orally active therapeutic agents.

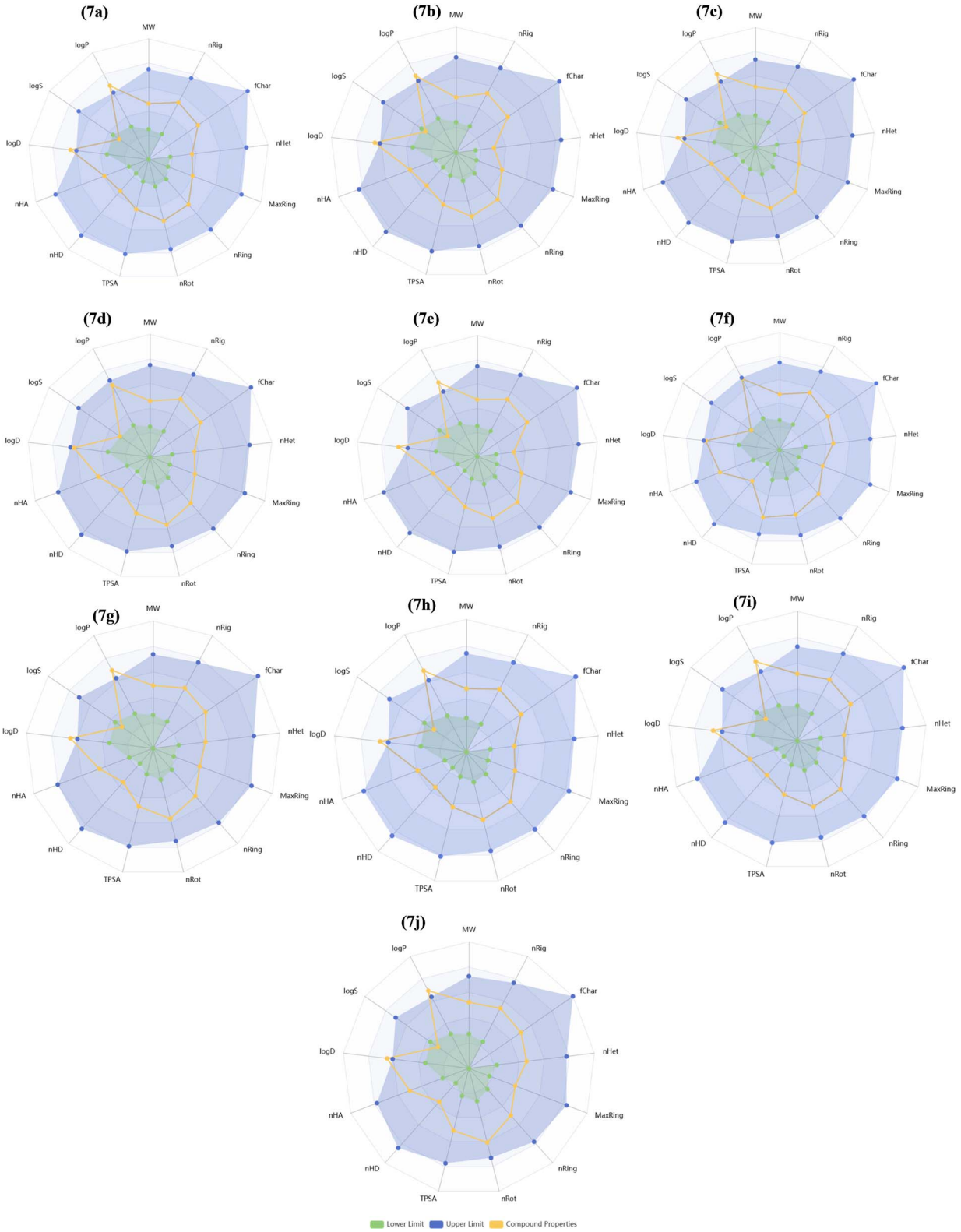

Fig. 8 Bioavailability radar plot of guanidine derivatives (**7a–j**).

The radar plots (Fig. 8) illustrated that all compounds (**7a–j**) fall within the optimal range for key drug-likeness parameters. Each compound complied with Lipinski's rule of five, showing molecular weights below 500 g mol^{-1}, two hydrogen bond donors, 4–7 hydrogen bond acceptors, and 6–8 rotatable bonds, signifying favorable oral bioavailability and molecular flexibility. These properties are necessary for optimal passive diffusion and receptor binding. The topological polar surface area (TPSA) for all compounds <100 $Å^2$, is ideal for blood–brain barrier penetration and gastrointestinal absorption.

All compounds exhibited high human intestinal absorption (HIA), ranging from 85.1–100%, indicating excellent oral bioavailability (Table 5). The Caco-2 permeability values for most derivatives fell within the optimum range (>0.9 log P_{app}), with compounds (**7a**), (**7b**), (**7e**), (**7g**), and (**7h**) demonstrating values >1.0, suggestive of efficient transcellular transport. Notably, compounds (**7c**) and (**7d**) showed slightly reduced Caco-2 permeability (0.828–0.835), and (**7f**) presented the lowest permeability (0.348), which could be attributed to enhanced polarity or steric hindrance due to the presence of nitro groups. Volume of distribution (VD) values for the most compounds were moderate to high (>1.0 L kg^{-1}), implying good tissue permeability. Compound (**7d**) and (**7e**) showed very low VD (0.011 L kg^{-1}), possibly reflecting their stronger plasma protein binding.

In case of blood–brain barrier (BBB) permeability, most compounds exhibited positive log BB values (>0.1), due to their high potential to cross the BBB. However, compound (**7d**) (log BB = −0.084) and (**7j**) (log BB = 0.003) were exceptions, reflecting lower CNS availability. CNS permeability (log PS) values were within the moderate range (−1.7 to −3.3), with (**7d**) and (**7g**) exhibiting the lowest values, further supporting reduced CNS exposure for these derivatives. Cytochrome P450 (CYP) profiling indicated that several compounds may act as enzyme inhibitors or substrates, suggesting negligible potential for metabolic liabilities and drug–drug interactions. Notably, compounds with halogen or methoxy groups showed interaction potential with CYP2C19, CYP2D6, and CYP3A4 isoforms. The predicted clearance (CL) rates were within the normal range (>0.5 mL min^{-1} kg^{-1}), indicating efficient elimination. However, compounds (**7a**) and (**7e**) exhibited prolonged retention in the body. While this may enhance therapeutic efficacy, it also raises concerns regarding potential accumulation and associated toxicity risks.

Importantly, none of the compounds were predicted to be hERG blockers or skin sensitizers, suggesting a low risk of cardiotoxicity and dermal adverse effects. However, AMES toxicity was predicted for compound (**7c**), (**7f**), and (**7h**), indicating potential mutagenicity. Despite this, the overall favorable ADMET profile, particularly the lack of hepatotoxicity, cardiotoxicity, and high CNS permeability, supports these compounds, especially the non-mutagenic ones, as promising candidates for further optimization and development.

3. Experimental

All reagents and chemicals used in this study were of analytical grade and sourced from Sigma-Aldrich. Solvents were dried and distilled using standard methods before use. Prior to use, solvents were dried and distilled through standard procedures. The melting points of the synthesized derivatives (**7a–j**) were measured using a StuartSMP3 melting point apparatus. FTIR spectra were recorded on a Thermo Fisher Scientific FT-IR spectrometer equipped with an ATR accessory, and the results were reported in cm^{-1}. Further structural characterization of the synthesized derivatives (**7a–j**) was conducted *via* NMR spectroscopy (^{1}H NMR spectra at 300 MHz and ^{13}C NMR at 75 MHz), utilizing a Bruker Avance spectrometer. Deuterated solvents (acetone and chloroform) were used for sample preparation, with tetramethyl silane (TMS) as an internal reference. Chemical shift values (δ) were reported in parts per million (ppm) and coupling constants (J) in hertz (Hz). The progression of reaction was observed by thin layer chromatography (TLC) on Merck aluminium-backed plates coated with silica gel Kiesel $60F_{254}$ (0.2 mm thickness). A mobile phase consisting of *n*-hexane and ethyl acetate (7 : 3) was employed. TLC spots were visualized under UV light at wavelengths of 254 and 365 nm. R_f values were calculated to assess compound purity and monitor the reaction course.

3.1. Protocol for the synthesis of guanidine derivatives (7a–j)

For the guanidine synthesis (**7a–j**), the thiourea precursors (**5a–d**) (1.1 mmol) and triethylamine (1.4 mmol) were dissolved in DMF solvent. The reaction mixture was cooled to 0 °C, and mercuric chloride ($HgCl_2$) (1.1 mmol) was added under vigorous stirring. After 30 minutes, substituted anilines (1.1 mmol) (**6a–f**) were added, and the reaction mixture was stirred at 25 °C for 18 hours. During the reaction, initially light yellow colored mixture gradually turned dark black, indicating desulfurization. Upon complete consumption of reactants, as observed by TLC, the reaction mixture was filtered to remove the black precipitate of mercuric sulfide. Ice chips were then poured into the filtrate and stirred for 20 minutes, resulting in the precipitation of the solid guanidine products. The solid was filtered, dried, and recrystallized from ethanol to obtain the desired products (**7a–j**).

3.1.1 *N*-(*N*′-(4-Chlorophenyl)-*N*-cyclopropylcarbamimidoyl) benzamide (7a).

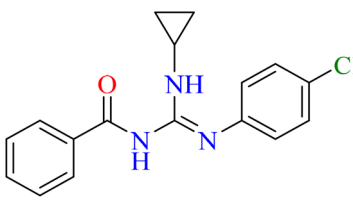

White crystals; mp.: 126–128 °C; yield: 81%; R_f: 0.55 (*n*-hexane : ethyl acetate, 7 : 3); FTIR (ATR, cm^{-1}), 3346, 3214 (N–H), 3088 (sp^2 C–H), 3010 (sp^3 C–H), 1678 (C=O, amide), 1643 (C=N), 1544 (C=C), 1341 (C–N); ^{1}H NMR (300 MHz, acetone-d_6) δ: 10.82 (s, 1H, NH), 8.40 (s, 1H, NH), 8.14 (d, 2H, ^3J = 7.2 Hz, aromatic), 7.70 (d, 2H, ^3J = 8.1 Hz, aromatic), 7.48–7.39 (m, 5H, aromatic), 2.92–2.83 (m, 1H, cyclopropyl C–H), 0.98–0.81 (m, 4H, cyclopropyl 2× CH_2); ^{13}C NMR (75 MHz, acetone-d_6) δ: 176.7 (C=O), 160.0 (C=N), 138.9, 137.3, 130.8, 128.2, 127.7, 125.4 (aromatic carbons), 22.2, 7.2 (cyclopropyl carbons). Anal. calcd for $C_{17}H_{16}ClN_3O$

[313.79]: C, 65.07; H, 5.14; N, 13.39%. Found: C, 65.09; H, 5.11; N, 13.40%.

3.1.2 *N*-(*N*′-(4-Bromophenyl)-*N*-cyclopropylcarbamimidoyl) benzamide (7b).

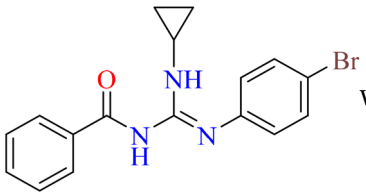

White crystals; mp.: 132–134 °C; yield: 86%; R_f: 0.56 (*n*-hexane : ethyl acetate, 7 : 3); FTIR (ATR, cm^{-1}), 3398, 3246 (N–H), 3088 (sp^2 C–H), 3007 (sp^3 C–H), 1659 (C=O, amide), 1646 (C=N), 1557 (C=C), 1257 (C–N); ^1H NMR (300 MHz, acetone-d_6) δ: 10.80 (s, 1H, NH), 8.32 (s, 1H, NH), 8.14 (d, 2H, ^3J = 6.9 Hz, aromatic), 7.66 (d, 2H, ^3J = 9 Hz, aromatic), 7.59–7.55 (m, 2H, aromatic), 7.49–7.36 (m, 3H, aromatic), 2.90–2.87 (m, 1H, cyclopropyl C–H), 1.00–0.82 (m, 4H, cyclopropyl 2× CH_2); ^{13}C NMR (75 MHz, acetone-d_6) δ: 176.7 (C=O), 160.0 (C=N), 138.9, 138.0, 131.2, 130.8, 128.9, 127.7, 125.6, (aromatic carbons), 22.1, 7.2 (cyclopropyl carbons). Anal. calcd for $C_{17}H_{16}BrN_3O$ [358.24]: C, 57.00; H, 4.50; N, 11.73%. Found: C, 57.03; H, 4.52; N, 11.70%.

3.1.3 *N*-(*N*-Cyclopropyl-*N*′-(*p*-tolyl)carbamimidoyl)benzamide (7c).

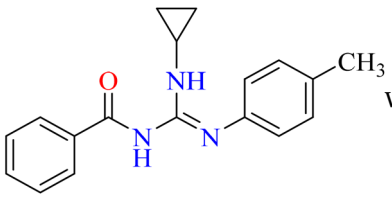

White crystals; mp.: 147–149 °C; yield: 89%; R_f: 0.59 (*n*-hexane : ethyl acetate, 7 : 3); FTIR (ATR, cm^{-1}), 3403, 3280 (N–H), 3025 (sp^2 C–H), 2920 (sp^3 C–H), 1676 (C=O, amide), 1638 (C=N), 1545 (C=C), 1261 (C–N); ^1H NMR (300 MHz, $CDCl_3$) δ: 10.86 (s, 1H, NH), 8.28–8.24 (m, 2H, aromatic), 7.49–7.36 (m, 4H, aromatic), 7.23–7.21 (m, 2H, aromatic), 2.40 (m, 1H, cyclopropyl C–H), 2.39 (s, 3H, OCH_3), 0.84–0.75 (m, 4H, cyclopropyl 2× CH_2); ^{13}C NMR (75 MHz, $CDCl_3$) δ: 178.1 (C=O), 169.5 (C=N), 133.8, 131.6, 129.8, 129.7, 129.1, 128.8, 128.0, 127.9 (aromatic carbons), 21.0 (cyclopropyl carbon), 21.0 (CH_3), 7.8 (cyclopropyl carbons). Anal. calcd for $C_{18}H_{19}N_3O$ [293.37]: C, 73.69; H, 6.53; N, 14.32%. Found: C, 73.68; H, 6.55; N, 14.35%.

3.1.4 *N*-(*N*-Cyclopropyl-*N*′-(4-methoxyphenyl)carbamimidoyl) benzamide (7d).

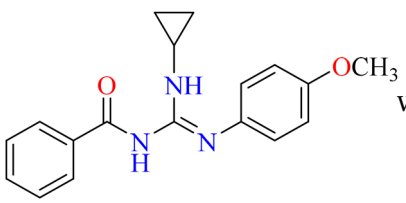

White crystals; mp.: 120–122 °C; yield: 91%; R_f: 0.53 (*n*-hexane : ethyl acetate, 7 : 3); FTIR (ATR, cm^{-1}), 3295, 3196 (N–H), 3010 (sp^2 C–H), 2836 (sp^3 C–H), 1664 (C=O, amide), 1628 (C=N), 1548 (C=C), 1241 (C–N); ^1H NMR (300 MHz, $CDCl_3$) δ: 10.60 (s, 1H, NH), 8.22 (d, 2H, ^3J = 3.6 Hz, aromatic), 7.49–7.37 (m, 5H, aromatic), 7.22 (d, 2H, ^3J = 8.1 Hz, aromatic), 2.98–2.75 (m, 1H, cyclopropyl C–H), 2.39 (s, 3H, OCH_3), 0.97–0.77 (m, 4H, cyclopropyl 2× CH_2); ^{13}C NMR (75 MHz, $CDCl_3$) δ: 177.0 (C=O), 167.3 (aromatic carbon), 161.5 (C=N), 135.5, 135.5, 133.2, 133.0, 130.1, 128.4, 126.1 (aromatic carbons), 55.5 (OCH_3), 26.9, 7.1 (cyclopropyl carbons). Anal. calcd for $C_{18}H_{19}N_3O_2$ [309.37]: C, 69.88; H, 6.19; N, 13.58%. Found: C, 69.89; H, 6.16; N, 13.61%.

3.1.5 *N*-(*N*-Cyclopropyl-*N*′-(3,4,5-trimethylphenyl)carbamimidoyl)benzamide (7e).

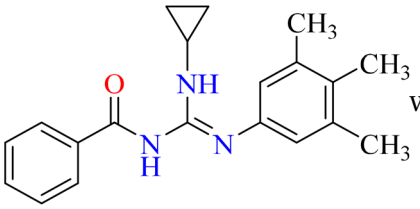

White crystals; mp.: 131–133 °C; yield: 86%; R_f: 0.55 (*n*-hexane : ethyl acetate, 7 : 3); FTIR (ATR, cm^{-1}), 3266, 3211 (N–H), 3014 (sp^2 C–H), 2918 (sp^3 C–H), 1664 (C=O, amide), 1615 (C=N), 1541 (C=C), 1233 (C–N); ^1H NMR (300 MHz, $CDCl_3$) δ: 10.70 (s, 1H, NH), 8.36 (s, 1H, NH), 7.87 (d, 1H, ^3J = 6.3 Hz, aromatic), 7.45–7.23 (m, 3H, aromatic), 6.95 (s, 2H, aromatic), 2.89–2.86 (m, 1H, cyclopropyl C–H), 2.29 (s, 6H, CH_3), 2.24 (s, 3H, CH_3), 1.01–0.74 (m, 4H, cyclopropyl 2× CH_2); ^{13}C NMR (75 MHz, $CDCl_3$) δ: 176.3 (C=O), 161.0 (C=N), 139.3, 135.9, 130.4, 129.0, 128.8, 128.2, 127.3 (aromatic carbons), 22.1 (cyclopropyl carbon), 20.1 (CH_3), 17.3 (CH_3), 7.4 (cyclopropyl carbons). Anal. calcd for $C_{20}H_{23}N_3O$ [321.42]: C, 74.74; H, 7.21; N, 13.07%. Found: C, 74.71; H, 7.23; N, 13.06%.

3.1.6 *N*-(*N*-Cyclopropyl-*N*′-(3-nitrophenyl)carbamimidoyl) benzamide (7f).

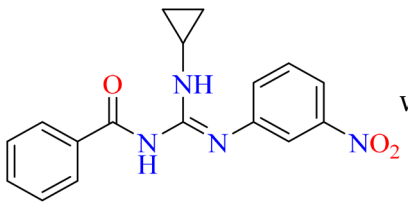

White crystals; mp.: 128–130 °C; yield: 76%; R_f: 0.44 (*n*-hexane : ethyl acetate, 7 : 3); FTIR (ATR, cm^{-1}), 3284, 3211 (N–H), 3094 (sp^2 C–H), 2944 (sp^3 C–H), 1673 (C=O, amide), 1627 (C=N), 1532 (C=C), 1222 (C–N); ^1H NMR (300 MHz, acetone-d_6) δ: 10.0 (s, 1H, NH), 8.79 (s, 1H, NH), 8.13–8.09 (m, 2H, aromatic), 7.68–7.63 (m, 3H, aromatic), 7.58–7.52 (m, 4H, aromatic), 2.82–2.75 (m, 1H, cyclopropyl C–H), 0.81–0.61 (m, 4H, cyclopropyl 2× CH_2); ^{13}C NMR (75 MHz, acetone-d_6) δ: 168.1 (C=O), 154.7 (C=N), 154.7, 132.8, 132.7, 132.6, 128.6, 128.5, 128.0 (aromatic carbons), 22., 5.9 (cyclopropyl carbons). Anal. calcd for $C_{17}H_{16}N_4O_3$ [324.34]: C, 62.95; H, 4.97; N, 17.27%. Found: C, 62.92; H, 4.98; N, 17.30%.

3.1.7 *N*-(*N*′-(4-Chlorophenyl)-*N*-cyclopropylcarbamimidoyl)-4-methoxybenzamide (7g).

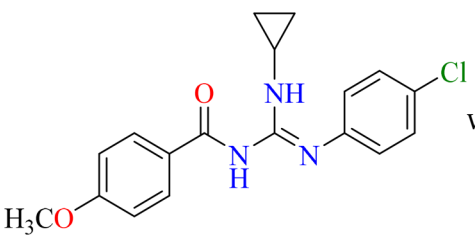

White crystals; mp.:

144–146 °C; yield: 83%; R_f: 0.45 (*n*-hexane : ethyl acetate, 7 : 3); FTIR (ATR, cm^{-1}), 3316, 3145 (N–H), 3031 (sp^2 C–H), 2935 (sp^3 C–H), 1681 (C=O, amide), 1631 (C=N), 1508 (C=C), 1241 (C–N); ^{1}H NMR (300 MHz, acetone-d_6) δ: 10.67 (s, 1H, NH), 8.09 (d, 2H, ^3J = 8.7 Hz, aromatic), 7.70 (d, 2H, ^3J = 8.1 Hz, aromatic), 7.44–7.40 (m, 2H, aromatic), 6.92 (dd, 2H, ^4J = 1.8 Hz , ^3J = 6.6 Hz, aromatic), 3.84 (s, 3H, CH_3), 2.88–2.83 (m, 1H, cyclopropyl C–H), 0.97–0.78 (m, 4H, cyclopropyl 2× CH_2); ^{13}C NMR (75 MHz, acetone-d_6) δ: 176.5 (C=O), 162.2 (aromatic carbon), 159.7 (C=N), 137.4, 131.5, 130.8, 128.6, 128.2, 125.1, 112.9 (aromatic carbons), 54.7 (OCH_3), 22.2, 7.2 (cyclopropyl carbons). Anal. calcd for $C_{18}H_{18}ClN_3O_2$ [343.81]: C, 62.88; H, 5.28; N, 12.22%. Found: C, 62.89; H, 5.26; N, 12.25%.

3.1.8 *N*-(*N*′-(4-Chlorophenyl)-*N*-cyclopropylcarbamimidoyl)-4-methylbenzamide (7h).

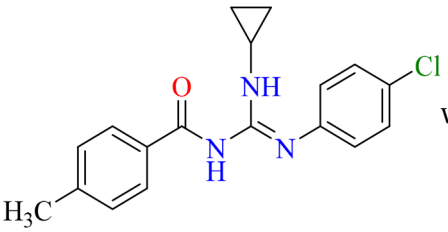

White crystals; mp.: 139–142 °C; yield: 79%; R_f: 0.48 (*n*-hexane : ethyl acetate, 7 : 3); FTIR (ATR, cm^{-1}), 3286, 3100 (N–H), 3007 (sp^2 C–H), 2923 (sp^3 C–H), 1681 (C=O, amide), 1635 (C=N), 1541 (C=C), 1254 (C–N); ^{1}H NMR (300 MHz, acetone-d_6) δ: 10.71 (s, 1H, NH), 8.34 (s, 1H, NH), 8.03 (d, 2H, ^3J = 8.1 Hz, aromatic), 7.71 (d, 2H, ^3J = 8.1 Hz, aromatic), 7.44–7.40 (m, 2H, aromatic), 7.20 (d, 2H, ^3J = 7.8 Hz, aromatic), 2.90–2.87 (m, 1H, cyclopropyl C–H), 2.36 (CH_3), 1.00–0.77 (m, 4H, cyclopropyl 2× CH_2); ^{13}C NMR (75 MHz, acetone-d_6) δ: 176.8 (C=O), 159.8 (C=N), 141.0, 137.4, 136.3, 129.0, 128.6, 128.3, 128.2, 125.2 (aromatic carbons), 22.2 (cyclopropyl carbon), 20.5 (CH_3), 7.2 (cyclopropyl carbon). Anal. calcd for $C_{18}H_{18}ClN_3O$ [327.81]: C, 65.95; H, 5.53; N, 12.82%. Found: C, 65.94; H, 5.54; N, 12.85%.

3.1.9 *N*-(*N*′-(4-Bromophenyl)-*N*-cyclopropylcarbamimidoyl)-4-methylbenzamide (7i).

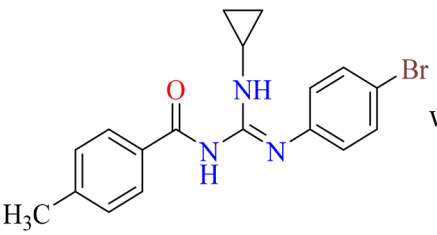

White crystals; mp.: 135–137 °C; yield: 87%; R_f: 0.46 (*n*-hexane : ethyl acetate, 7 : 3); FTIR (ATR, cm^{-1}), 3286, 3094 (N–H), 3004 (sp^2 C–H), 2923 (sp^3 C–H), 1629 (C=O, amide), 1636 (C=N), 1484 (C=C), 1246 (C–N); ^{1}H NMR (300 MHz, $CDCl_3$) δ: 10.69 (s, 1H, NH), 8.03 (d, 2H, ^3J = 8.1 Hz, aromatic), 7.66 (d, 2H, ^3J = 8.4 Hz, aromatic), 7.58–7.54 (m, 2H, aromatic), 7.20 (d, 2H, ^3J = 7.8 Hz, aromatic), 2.89–2.85 (m, 1H, cyclopropyl C–H), 2.36 (CH_3), 0.99–0.77 (m, 4H, cyclopropyl 2× CH_2); ^{13}C NMR (75 MHz, $CDCl_3$) δ: 176.8 (C=O), 159.7 (C=N), 141.0, 136.3, 131.2, 129.0, 129.0, 128.4, 128.4, 125.5 (aromatic carbons), 22.2 (cyclopropyl carbon), 20.5 (CH_3), 7.2 (cyclopropyl carbon). Anal. calcd for $C_{18}H_{18}BrN_3O$ [372.27]: C, 58.08; H, 4.87; N, 11.29%. Found: C, 58.10; H, 4.88; 11.27%.

3.1.10 *N*-(*N*′-(4-Chlorophenyl)-*N*-cyclopropylcarbamimidoyl)-3,4-dimethoxybenzamide (7j).

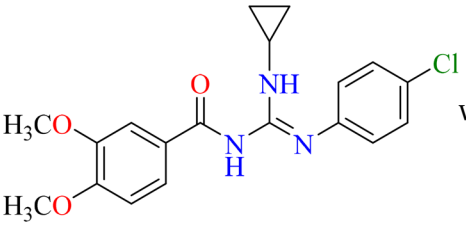

White crystals; mp.: 151–153 °C; yield: 85%; R_f: 0.51 (*n*-hexane : ethyl acetate, 7 : 3); FTIR (ATR, cm^{-1}), 3395, 3084 (N–H), 3014 (sp^2 C–H), 2952 (sp^3 C–H), 1682 (C=O, amide), 1652 (C=N), 1560 (C=C), 1266 (C–N); ^{1}H NMR (300 MHz, $CDCl_3$) δ: 7.73 (s, 4H, aromatic), 7.44–7.40 (m, 2H, aromatic), 6.94 (d, 1H, ^3J = 9 Hz, aromatic), 6.85 (OCH_3), 3.81 (OCH_3), 2.87–2.83 (m, 1H, cyclopropyl C–H), 0.97–0.77 (m, 4H, cyclopropyl 2× CH_2); ^{13}C NMR (75 MHz, $CDCl_3$) δ: 176.3 (C=O), 164.4 (C=N), 151.9, 148.4, 139.2, 133.4, 132.7, 128.1, 125.3, 122.3, 112.1, 110.3 (aromatic carbons), 55.1, 54.8 (OCH_3), 22.2, 7.2 (cyclopropyl carbons). Anal. calcd for $C_{19}H_{20}ClN_3O_3$ [373.84]: C, 61.05; H, 5.39; N, 11.24%. Found: C, 61.07; H, 5.38; N, 11.27%.

3.2. DNA binding protocol

SS-DNA, purchased from Sigma-Aldrich, was used as received without any additional purification. A stock solution of DNA was prepared using deionized water and subsequently diluted to suitable concentrations for spectrophotometric measurements. DNA concentration was determined by measuring absorbance at 260 nm with a UV-Visible spectrophotometer, applying the Beer–Lambert law: $c = A_{260}/(\varepsilon \times l)$, where ε is 6600 M^{-1} cm^{-1} and the path length (l) is 1 cm. The A_{260}/A_{280} absorbance ratio was determined to be 1.87, indicating low levels of protein contamination and confirming the suitability of the DNA for binding studies. Fresh dilutions of SS-DNA in the micromolar range were prepared for each experiment. The guanidine derivatives (**7a–j**) were dissolved in methanol at a concentration of 50 μM, and their baseline UV absorption spectra were obtained before adding DNA. UV-Vis titration experiments were carried out in duplicate by maintaining a constant compound concentration while gradually increasing the SS-DNA concentration from 5 to 40 μM. All spectral measurements were recorded using a Shimadzu 1700 UV-Visible spectrophotometer, and the binding parameters are reported as mean ± SEM (n = 2).

3.3. Molecular docking

Docking simulations were performed by employing AutoDock Vina 1.5.7 tools[29] to evaluate the interaction of guanidine derivatives (**7a–j**) with DNA. The crystal structures of DNA (PDB ID: 3EY0) was retrieved from Protein Data Bank *via* the link: **https://doi.org/10.2210/pdb6XVJ/pdb**. Prior to docking, the protein was prepared using AutoDock Tools by removing crystallographic water molecules, adding polar hydrogen atoms, and assigning Kollman charges. A docking grid was generated around the active site, guided by the position of the

co-crystallized ligand, and its coordinates and dimensions were specified in a configuration file. The ligand originally present in the crystal structure was removed before saving the DNA model in PDBQT format. The synthesized guanidines (**7a–j**) were geometrically optimized using Gaussian 09 (ref. 30) software (B3LYP/6-31G(d)). Then these optimized structures were initially saved in PDB format using GaussView 6.0 and subsequently converted to PDBQT files for docking studies. Docking simulations were executed *via* the command-line interface, and the resulting binding poses and interactions were analyzed and visualized using Discovery Studio.[31] While molecular docking provides valuable insights into the potential binding modes and affinities of the compounds with DNA, it is important to acknowledge its limitations. Docking simulations typically treat DNA as a rigid structure and do not fully account for solvent effects, ionic strength, or dynamic conformational changes that occur under physiological conditions. As a result, docking scores and predicted binding poses should be interpreted qualitatively rather than quantitatively. To strengthen the conclusions, docking results were complemented by experimental studies, including UV-Vis titrations assay, which provide direct evidence of DNA-binding interactions and validate the theoretical predictions.

3.4. Density functional theory

DFT calculations were carried out using GaussView 6.0 software with the B3LYP functional and 6-31G(d) basis set.[32] All computations were conducted in the gas phase to obtain optimized geometries, electronic properties, and energy-related parameters.

3.5. ADMET

The ADMET properties of the guanidine derivatives (**7a–j**) were assessed using the online platforms pkCSM[33] and ADMET lab 3.0.[34] Canonical SMILES representations for each compound were generated using ChemDraw 22.0, and key physicochemical properties and pharmacokinetic potential were systematically predicted.

4. Conclusions

A novel series of guanidine derivatives (**7a–j**) was synthesized and evaluated as potential DNA-binding agents. Spectroscopic and docking studies revealed strong affinities ($K_b = 10^4$ to 10^5 M^{-1}), with compound (**7i**) (4-Me, 4-Br) showing the highest binding constant ($3.49 \times 10^5 \pm 0.04$ M^{-1}), favorable thermodynamics, and the best docking score (-8.9 kcal mol^{-1}). DFT analysis indicated optimal electronic properties, while ADMET predictions suggested overall drug-likeness but also flagged potential risks such as AMES toxicity and prolonged retention, underscoring the need for scaffold optimization. Although DNA was selected as the primary target based on precedent for guanidine minor-groove binders, selectivity toward other biomacromolecules and effects on non-cancerous cells remain to be clarified. Beyond DNA binding, these scaffolds may have broader therapeutic potential, including synergy with current chemotherapeutics, overcoming resistance, and application in multi-target drug design. Importantly, the present work establishes DNA binding as a mechanistic foundation for guanidine derivatives and future studies will therefore focus on selectivity profiling, cytotoxicity in cancer *versus* normal cells, *in vivo* validation, and scaffold optimization through the introduction of metabolically cleavable substituents, balanced lipophilicity, and refined electronic features to enhance pharmacokinetics and safety, thereby supporting progression toward preclinical development.

Author contributions

Hina Zaman: investigation, methodology, writing – original draft, data curation, formal analysis. Aamer Saeed: conceptualization, supervision, validation, writing – review & editing. Uzma Azam: data curation, formal analysis, investigation. Ghulam Shabir, Madiha Irfan: data curation, formal analysis, investigation, formal analysis, validation. Basant Farag: data curation, validation, writing – review. Hesham R. El-Seedi: data curation, formal analysis, funding resources.

Conflicts of interest

The authors declare that there are no conflicts of interest.

Data availability

The datasets generated and/or analyzed during the current study are available from the corresponding author upon reasonable request.

Supplementary information: All SI material related to this work is available. See DOI: **https://doi.org/10.1039/d5ra05647k**.

References

1 S. D. Khalaf, M. M. Mahdi and R. S. Mahmood, The cancer: types, the mechanism of caner growth and diagnosis: A, *World J. Pharm. Res.*, 2024, **3**(3), 274–282.
2 D. Zhang, M. Li, A. M. Rahman, Z. Liu and Y. Lu, Exploring the DNA-binding and anticancer potential of polypyridyl ruthenium (II) complexes, *J. Mol. Struct.*, 2025, **1321**, 140044.
3 M. Ljungman, Targeting the DNA damage response in cancer, *Chem. Rev.*, 2009, **109**(7), 2929–2950.
4 K. Gurova, New hopes from old drugs: revisiting DNA-binding small molecules as anticancer agents, *Future Oncol.*, 2009, **5**(10), 1685–1704.
5 R. Palchaudhuri and P. J. Hergenrother, DNA as a target for anticancer compounds: methods to determine the mode of binding and the mechanism of action, *Curr. Opin. Biotechnol.*, 2007, **18**(6), 497–503.
6 J. W. Shaw, D. H. Grayson and I. Rozas, Synthesis of guanidines and some of their biological applications, *Guanidines as Reagents and Catalysts I*, Springer International Publishing, Cham, 2017, pp. 1–51.
7 F. Saczewski and Ł. Balewski, Biological activities of guanidine compounds, *Expert Opin. Ther. Pat.*, 2009, **19**(10), 1417–1448.

8 A. N. Muttathukattil, S. Srinivasan, A. Halder and G. Reddy, Role of guanidinium-carboxylate ion interaction in enzyme inhibition with implications for drug design, *J. Phys. Chem. B*, 2019, **123**(44), 9302–9311.
9 L. Wang, B. Zhou, Y. Du, M. Bai, X. Xu, Y. Guan and X. Liu, Guanidine derivatives leverage the antibacterial performance of bio-based polyamide PA56 fibres, *Polymers*, 2024, **16**, 2707.
10 R. Fukutomi, A. Tanatani, H. Kakuta, N. Tomioka, A. Itai, Y. Hashimoto, K. Shudo and H. Kagechika, Aromatic layered guanidines bind sequence-specifically to DNA minor groove with precise fit, *Tetrahedron Lett.*, 1998, **39**(36), 6475–6478.
11 R. K. Arafa, M. A. Ismail, M. Munde, W. D. Wilson, T. Wenzler, R. Brun and D. W. Boykin, Novel linear triaryl guanidines, *N*-substituted guanidines and potential prodrugs as antiprotozoal agents, *Eur. J. Med. Chem.*, 2008, **43**(12), 2901–2908.
12 A. R. Gomes, C. L. Varela, A. S. Pires, E. J. Tavares-da-Silva and F. M. Roleira, Synthetic and natural guanidine derivatives as antitumor and antimicrobial agents: a review, *Bioorg. Chem.*, 2023, **138**, 106600.
13 P. S. Nagle, S. J. Quinn, J. M. Kelly, D. H. O'Donovan, A. R. Khan, F. Rodriguez, B. Nguyen, W. D. Wilson and I. Rozas, Understanding the DNA binding of novel non-symmetrical guanidinium/2-aminoimidazolinium derivatives, *Org. Biomol. Chem.*, 2010, **8**(24), 5558–5567.
14 F. Rodríguez, I. Rozas, M. Kaiser, R. Brun, B. Nguyen, W. D. Wilson, R. N. García and C. Dardonville, New bis (2-aminoimidazoline) and bisguanidine DNA minor groove binders with potent in vivo antitrypanosomal and antiplasmodial activity, *J. Med. Chem.*, 2008, **51**(4), 909–923.
15 H. Zaman, A. Saeed, H. Ismail, S. Anwaar, M. Latif, M. Z. Hashmi and H. R. El-Seedi, Novel pyrimidine linked acyl thiourea derivatives as potent α-amylase and proteinase K inhibitors: design, synthesis, molecular docking and ADME studies, *RSC Adv.*, 2024, **14**(45), 33235–33246.
16 H. Zaman, A. Saeed, T. ul Muntaha, H. Ismail, S. K. Hashmi, U. e Rubab, A. Alsharif, M. M. Soliman, A. Gaber and A. Mumtaz, Development of novel cyclopropyl tethered iminothiazolidinone-isatin hybrids as effective multi target intestinal alkaline phosphatase, urease and α-glucosidase inhibitors, *Int. J. Biol. Macromol.*, 2025, 143377.
17 H. Zaman, A. Saeed, T. ul Muntaha, H. Ismail and M. Rashid, Novel Cyclopropyl Appended 1, 3-Thiazole-2-Imines as Multi-Target Agents: Design, Synthesis, Biological Evaluation and Computational Studies, *Asian J. Org. Chem.*, 2025, **14**(2), e202400598.
18 T. T. Talele, The "cyclopropyl fragment" is a versatile player that frequently appears in preclinical/clinical drug molecules, *J. Med. Chem.*, 2016, **59**(19), 8712–8756.
19 H. Zaman, A. Saeed, H. Ismail and M. Rashid, Unveiling the cyclopropyl appended acyl thiourea derivatives as antimicrobial, α-amylase and proteinase K inhibitors: design, synthesis, biological evaluation, molecular docking, DFT and ADMET studies, *Arch. Biochem. Biophys.*, 2025, **765**, 110304.
20 L. H. Hurley, DNA and its associated processes as targets for cancer therapy, *Nat. Rev. Cancer*, 2002, **2**(3), 188–200.
21 G. Magdy, F. Belal, A. F. A. Hakiem and A. M. Abdel-Megied, Salmon sperm DNA binding study to cabozantinib, a tyrosine kinase inhibitor: multi-spectroscopic and molecular docking approaches, *Int. J. Biol. Macromol.*, 2021, **182**, 1852–1862.
22 P. O'Sullivan and I. Rozas, Understanding the Guanidine-Like Cationic Moiety for Optimal Binding into the DNA Minor Groove, *ChemMedChem*, 2014, **9**(9), 2065–2073.
23 C. Bailly, A. W. Cuthbert, D. Gentle, M. R. Knowles and M. J. Waring, Sequence-selective binding of amiloride to DNA, *Biochemistry*, 1993, **32**(10), 2514–2524.
24 E. A. Lewis, M. Munde, S. Wang, M. Rettig, V. Le, V. Machha and W. D. Wilson, Complexity in the binding of minor groove agents: netropsin has two thermodynamically different DNA binding modes at a single site, *Nucleic Acids Res.*, 2011, **39**(22), 9649–9658.
25 E. O. Akintemi, K. K. Govender and T. Singh, A DFT study of the chemical reactivity properties, spectroscopy and bioactivity scores of bioactive flavonols, *Comput. Theor. Chem.*, 2022, **1210**, 113658.
26 V. Kairys, L. Baranauskiene, M. Kazlauskiene, D. Matulis and E. Kazlauskas, Binding affinity in drug design: experimental and computational techniques, *Expert Opin. Drug Discovery*, 2019, **14**(8), 755–768.
27 P. Guo, A. A. Farahat, A. Paul, N. K. Harika, D. W. Boykin and W. D. Wilson, Compound shape effects in minor groove binding affinity and specificity for mixed sequence DNA, *J. Am. Chem. Soc.*, 2018, **140**(44), 14761–14769.
28 P. G. Baraldi, A. Bovero, F. Fruttarolo, D. Preti, M. A. Tabrizi, M. G. Pavani and R. Romagnoli, DNA minor groove binders as potential antitumor and antimicrobial agents, *Med. Res. Rev.*, 2004, **24**(4), 475–528.
29 O. Trott and A. J. Olson, AutoDock Vina: improving the speed and accuracy of docking with a new scoring function, efficient optimization, and multithreading, *J. Comput. Chem.*, 2010, **31**(2), 455–461.
30 M. Frisch, G. Trucks, H. Schlegel, G. Scuseria, M. Robb, J. Cheeseman, G. Scalmani, V. Barone, B. Mennucci and G. Petersson, *Gaussian 09 (Versions A.01 and D.01)*, Gaussian. Inc., Wallingford CT, 2009.
31 D. S. Biovia, *Discovery Studio*, Dassault Systèmes BIOVIA, 2016.
32 R. Dennington, T. A. Keith and J. M. Millam, *GaussView 6.0. 16*, Semichem Inc., Shawnee Mission, KS, USA, 2016, pp. , pp. 143–150.
33 D. E. Pires, T. L. Blundell and D. B. Ascher, pkCSM: predicting small-molecule pharmacokinetic and toxicity properties using graph-based signatures, *J. Med. Chem.*, 2015, **58**(9), 4066–4072.
34 L. Fu, S. Shi, J. Yi, N. Wang, Y. He, Z. Wu, J. Peng, Y. Deng, W. Wang and C. Wu, ADMETlab 3.0: an updated comprehensive online ADMET prediction platform enhanced with broader coverage, improved performance, API functionality and decision support, *Nucleic Acids Res.*, 2024, 422–431.